

# Combined Spectroscopy and Electrical Characterization of La:BaSnO<sub>3</sub> Thin Films and Heterostructures

Arnaud P. Nono Tchiomo,<sup>1,2</sup> Emanuela Carleschi,<sup>1</sup> Aletta R. E. Prinsloo,<sup>1</sup> Wilfried Sigle,<sup>3</sup> Peter A. van Aken,<sup>3</sup> Jochen Mannhart,<sup>3</sup> Prosper Ngabonziza,<sup>1,3,\*</sup> and Bryan P. Doyle<sup>1,†</sup>

<sup>1</sup>*Department of Physics, University of Johannesburg,  
P.O. Box 524 Auckland Park 2006, Johannesburg, South Africa*

<sup>2</sup>*Van der Waals-Zeeman Institute, Institute of Physics,  
Science Park 904, 1098 XH Amsterdam, The Netherlands*

<sup>3</sup>*Max Planck Institute for Solid State Research, Heisenbergstr. 1, 70569 Stuttgart, Germany*  
(Dated: March 14, 2024)

For La-doped BaSnO<sub>3</sub> thin films grown by pulsed laser deposition, we combine chemical surface characterization and electronic transport studies to probe the evolution of electronic states in the band structure for different La-doping content. Systematic analyses of spectroscopic data based on fitting the core electron line shapes help to unravel the composition of the surface as well as the dynamics associated with increasing doping. This dynamics is observed with a more pronounced signature in the Sn 3d core level, which exhibits an increasing asymmetry to the high binding energy side of the peak with increasing electron density. Our results expand current understanding of the interplay between the doping concentration, electronic band structure and transport properties of epitaxial La:BaSnO<sub>3</sub> films.

The perovskite La-doped BaSnO<sub>3</sub> (La:BaSnO<sub>3</sub>) is a novel transparent oxide semiconductor that exhibits outstanding room temperature (RT) electron mobility ( $\mu_e$ ) with high carrier density together with a high optical transmittance [1–3]. Owing to its unique electronic and optical properties, La:BaSnO<sub>3</sub> has the potential for applications in transparent electronics [4–7], photovoltaics [8–11], as well as in thermoelectric [12–15] and multifunctional perovskite-based optoelectronic devices [10, 16, 17]. Furthermore, its low-power consumption combined with its ability to be heavily doped and its good stability at high temperatures make La:BaSnO<sub>3</sub> a suitable material for integration in thermally stable capacitors, field effect transistors and power electronic devices [3, 4, 17–19].

The discovery of a RT  $\mu_e$  of 320 cm<sup>2</sup> V<sup>-1</sup>s<sup>-1</sup> (with corresponding carrier density,  $n = 8 \times 10^{19}$  cm<sup>-3</sup>) in La:BaSnO<sub>3</sub> single crystals [1–3] stimulated intense investigation into this material [4]. Particularly, the potential of La:BaSnO<sub>3</sub> for device applications and heterostructures triggered considerable interests in thin films grown from this compound [5–7, 15, 17, 19–38]. However, the reported  $\mu_e$  in La:BaSnO<sub>3</sub> thin films have only reached a maximum value of 183 cm<sup>2</sup> V<sup>-1</sup>s<sup>-1</sup> ( $n \simeq 1.2 \times 10^{20}$  cm<sup>-3</sup>) for epitaxial films grown by molecular beam epitaxy (MBE) [33]. Other growth techniques resulted in the following electron mobilities: 140 cm<sup>2</sup> V<sup>-1</sup>s<sup>-1</sup> ( $n \simeq 5.2 \times 10^{20}$  cm<sup>-3</sup>) for pulsed laser deposition (PLD) [27], 121 cm<sup>2</sup> V<sup>-1</sup>s<sup>-1</sup> ( $n \simeq 4.0 \times 10^{20}$  cm<sup>-3</sup>) for high-pressure magnetron sputtering [36], and 53 cm<sup>2</sup> V<sup>-1</sup>s<sup>-1</sup> ( $n \simeq 2.0 \times 10^{20}$  cm<sup>-3</sup>) for chemical solution deposition [39]. Various strategies to improve the mobility in La:BaSnO<sub>3</sub> epitaxial films have been explored. Such efforts include, for example, incorporation of undoped BaSnO<sub>3</sub> buffer layers to compensate for the lattice mismatch

between the substrate and the active La:BaSnO<sub>3</sub> top layers [7, 19, 26, 33], adsorption-controlled MBE for improved stoichiometry control [31–33, 40], very high-temperature grown insulating buffer layer to reduce the density of threading dislocations [27], and post growth annealing processes [22, 24, 41]. Besides the ongoing efforts for RT  $\mu_e$  improvement, in order to gain a better understanding of the conduction mechanisms in La:BaSnO<sub>3</sub> films, it is important to establish a proper correlation between the transport characteristics and the behavior of the electronic states in the conduction band. This is crucial because the high ambient  $\mu_e$  in La:BaSnO<sub>3</sub> has been proposed to originate from both the small effective mass of the electrons at the conduction band minimum (CBM) [25, 42], which is associated with the largely dispersive Sn-5s conduction band, and the low optical phonon scattering rate [19, 43].

Although several studies used photoemission spectroscopy techniques to investigate the electronic structure of La:BaSnO<sub>3</sub> films [32, 43–46], only few reports have combined electronic transport and spectroscopic studies to explore the evolution of electronic states in La:BaSnO<sub>3</sub> films and heterostructures at different La-doping levels [32, 43]. In particular, recent *ex-situ* hard x-ray photoemission spectroscopy (HAXPES) experiments on La:BaSnO<sub>3</sub> films demonstrated that both the CBM and the valence band maximum (VBM), as well as the core electrons are effectively modified with increasing carrier density [32]. Thus, this result call for additional combined spectroscopic and electrical characterizations to facilitate more quantitative exploration of the evolution of the intrinsic properties of La:BaSnO<sub>3</sub> films and heterostructures at different doping levels.

In the present paper we combine chemical surface analysis as a function of La doping using x-ray photoelec-

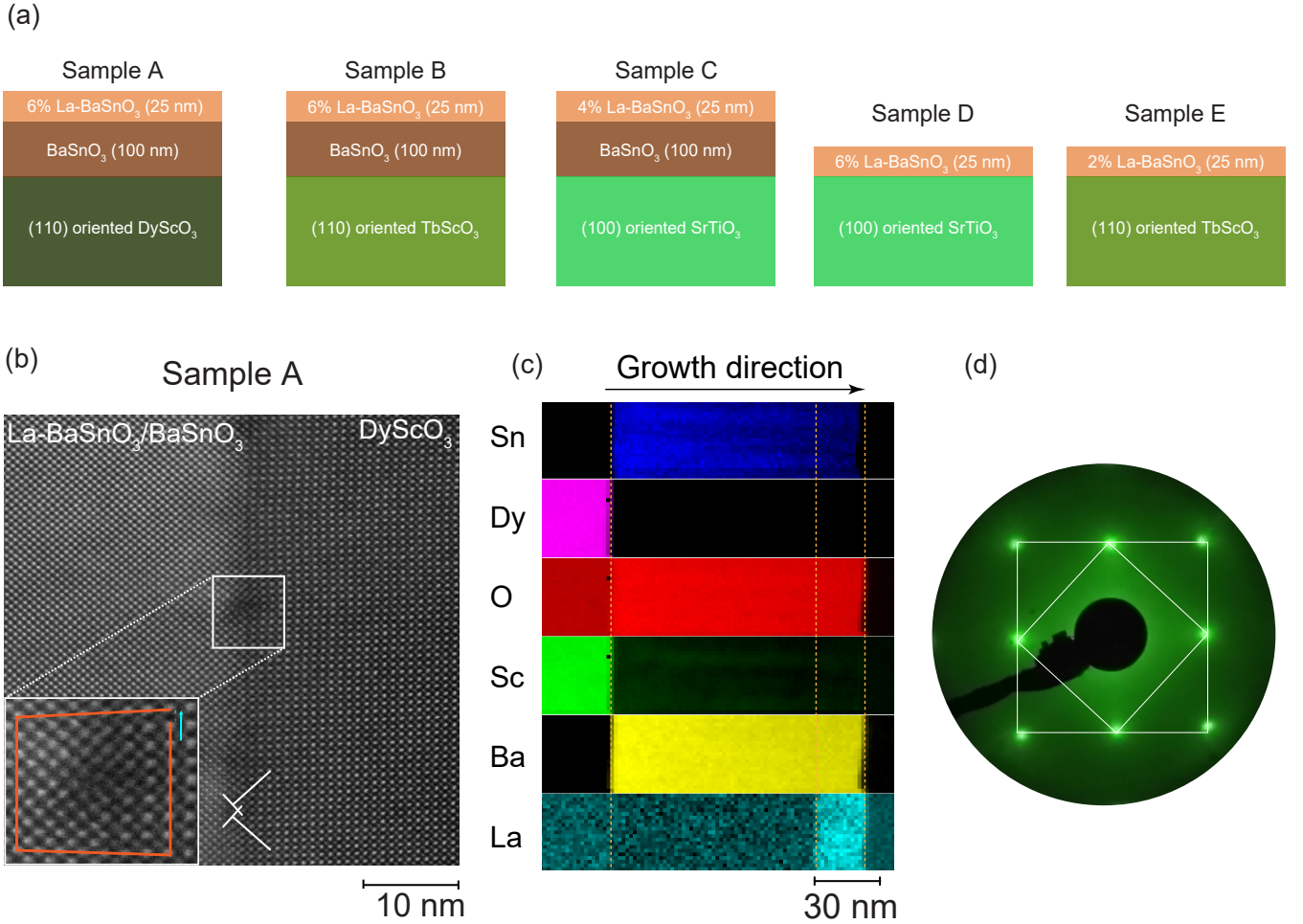


FIG. 1. (a) Schematic layout of the different thin film samples investigated in this study. (b) High-resolution scanning transmission electron microscopy (HRSTEM) image of a representative La:BaSnO<sub>3</sub>/BaSnO<sub>3</sub> heterostructure (sample A). Misfit dislocations indicated by the  $\perp$  symbols characterize the relaxed interface between the film and the (110) oriented DyScO<sub>3</sub> substrate. The inset represents a high magnification around one of the misfits delimited by the white rectangle, where a lack of closure of the Burgers circuit is seen (orange rectangular-like contour). (c) Electron energy-loss spectroscopy (EELS) elemental mapping for the sample A showing the distribution of the elements in the sample. The signal is divided into regions as indicated by the dashed orange lines. The residual color in the La plot is noise. (d) A representative low energy electron diffraction (LEED) image taken at 48 eV displaying a clean La:BaSnO<sub>3</sub> (001) surface. The diffraction spots form square lattices (white rectangle drawn on the image) in reciprocal space.

tron spectroscopy (XPS) and electronic transport studies to explore the evolution of the electronic states in La:BaSnO<sub>3</sub> films and heterostructures. From the transport measurements, we extract the transport characteristics, as well as  $n$  and  $\mu_e$  of the La:BaSnO<sub>3</sub> samples. The surface properties of these samples are subsequently investigated using spectroscopic techniques. A direct connection between the electronic transport characteristics and the spectroscopic data is demonstrated. We used XPS as a probing tool to measure the changes in the films spectra associated with the increasing amount of La<sup>3+</sup> dopant. Through the analysis and systematic fits of the core XPS spectra, we are able to extract the binding energy values of the constituent elements along with the associated oxidation states. These data are consis-

tent with the electron energy loss spectroscopy (EELS) data, as well as with referenced database. By increasing the doping concentration, we observe shifts of the valence band leading edges toward higher binding energies, as well as increases in the states in the conduction band. More importantly, we provide a quantitative understanding of the effect of conduction band filling in La:BaSnO<sub>3</sub> films and heterostructures. This effect is manifested by an increasing asymmetry in the line shape of the Sn 3d core spectra and leads to considering additional plasmon satellite peak in the analysis of Sn 3d spectra.

Epitaxial La:BaSnO<sub>3</sub> films and heterostructures (labeled sample A to E) were prepared by PLD ( $\lambda = 248$  nm). Prior to deposition, the (100) oriented SrTiO<sub>3</sub>, (110) oriented DyScO<sub>3</sub> and TbScO<sub>3</sub> crystalline sub-

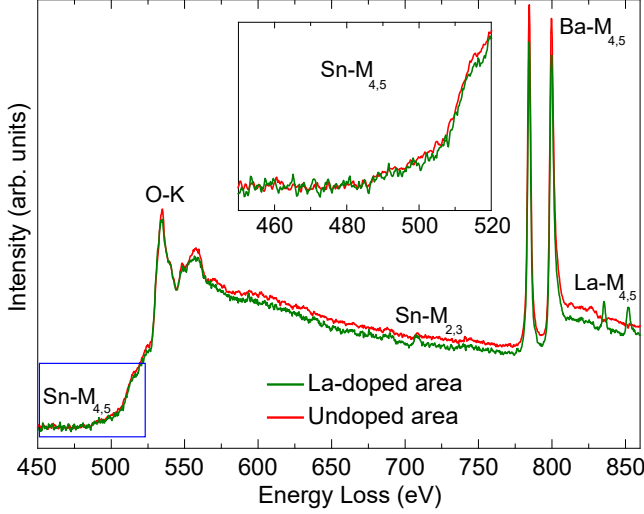


FIG. 2. Electron energy loss spectra of a representative La:BaSnO<sub>3</sub>/BaSnO<sub>3</sub> heterostructure. Two regions in the specimen were investigated: an area with only BaSnO<sub>3</sub> (red curve) and another with only La:BaSnO<sub>3</sub> (green curve). The inset shows the enlargement of the region around the Sn-M<sub>4,5</sub> ionized edge delimited by the blue rectangle.

strates ( $5 \times 5 \times 1$  mm<sup>3</sup>) were terminated in situ at 1300°C using a CO<sub>2</sub> laser substrate heating system [47]. Figure 1(a) depicts a schematic view of the sample types investigated. The films were grown from La:BaSnO<sub>3</sub> targets of 2%, 4% and 6% La doping contents. Details about the growth and systematic characterization of the films are provided in Ref. [27].

Electrical transport properties were measured in a physical property measurement system (PPMS) in a van der Pauw geometry obtained by wire bonding aluminum wires to the samples' corners [see Fig. S1 of the supplementary information]. The carrier concentration,  $n$ , and the electron mobility,  $\mu_e$ , were determined following the procedure discussed elsewhere [27, 48–50]. The La:BaSnO<sub>3</sub> samples analyzed here in both spectroscopy and transport experiments have carrier concentration ranging from  $n = 1.24$  to  $4.92 \times 10^{20}$  cm<sup>-3</sup> at room temperature [See more details in Table S1 of the supplemental information].

Following the procedure described in Ref. [51], the samples were systematically cleaned in ultra-high vacuum (UHV) before photoemission experiments. The surface structure of the samples was characterized using low-energy electron diffraction (LEED) [see Fig. S2(b) in supplementary information]. The surface of clean La:BaSnO<sub>3</sub> (001) surface showed a stable  $1 \times 1$  surface structure [Fig. 1(d)]. The diffraction spots form square lattices in reciprocal space corresponding to the cubic lattice structure of BaSnO<sub>3</sub> in real space, thus indicating the high crystallinity of the films [52]. The cleanliness of the samples was checked by monitoring the LEED patterns

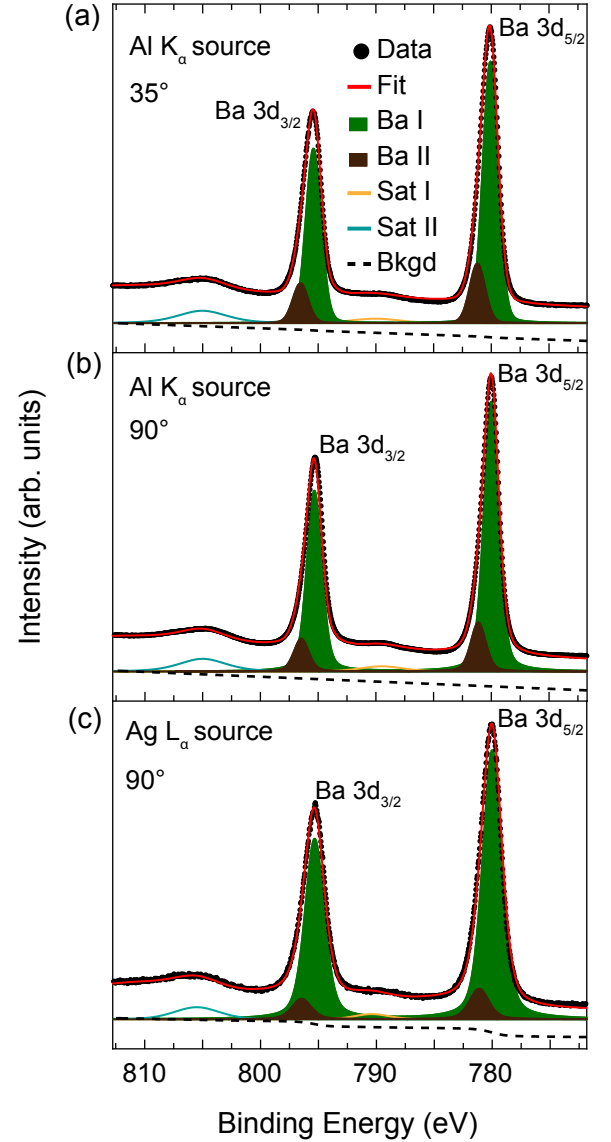


FIG. 3. Angle- and energy-dependent XPS spectra of the Ba 3d core level for the sample B. After subtracting a Shirley background (black dashed lineshape), the Ba 3d core lines are fitted (red lineshape) with two Voigt doublet peaks. The spectra in (a) and (b) were acquired with an Al K<sub>α</sub> anode (Al K<sub>α</sub> source) at 35° and 90° take-off angles, respectively. The spectrum in (c) was measured with an Ag L<sub>α</sub> anode (Ag L<sub>α</sub> source) at 90° take-off angle. Two satellite features (cyan and orange peaks) are resolved in the spectra. The peak heights were normalized for clarity.

directly after an annealing cycle, and also by comparing the XPS survey scans before and after cleaning [see Fig. S2 in supplementary information].

Figure 1(b) shows a representative scanning transmission electron microscopy (STEM) image of the investigated La:BaSnO<sub>3</sub> heterostructure (sample A). To check the stoichiometry of the samples, EELS measurements were performed on the cross section of the samples dur-

TABLE I. Peak ratios for angle-dependent XPS of the Ba 3d spectra.

	Peak assignment	Peak position ( $\pm 0.05$ eV)	Relative intensity ( $\pm 1$ %)	FWHM ( $\pm 0.05$ eV)
35°	Ba I	780.08	82	1.58
Al anode	Ba II	781.21	18	1.58
90°	Ba I	780.00	85	1.53
Al anode	Ba II	781.13	15	1.53
90°	Ba I	780.00	90	1.97
Ag anode	Ba II	781.13	10	1.97

ing STEM characterization. Figure 1(c) displays a representative EELS elemental mapping (atomic layer distribution) of the sample A for a total layer thickness of 120 nm of which the La-doped layer is 25 nm thick. The black color suggests a zero intensity, whereas the other colors indicate the presence of different elements (La, Ba, Sn, Dy, Sc, O) that are resolved in the scanned region.

Sn plays a key role in the structural and electronic transport characteristics of La:BaSnO<sub>3</sub> [2, 29, 53]. The loss of Ba:Sn stoichiometry in the nominal ratio 1:1 could result in additional defects in the films and hinder the desired electrical properties [32, 33]. The Ba:Sn stoichiometry in the grown films was examined by investigating the oxidation state of the Sn. Figure 2 shows EELS spectra of two regions of a representative La:BaSnO<sub>3</sub>/BaSnO<sub>3</sub> heterostructure, where the ionized edges of La-M<sub>4,5</sub>, Ba-M<sub>4,5</sub> and Sn-M<sub>4,5</sub> (corresponding to the excitation of 3d states), Sn-M<sub>2,3</sub> (corresponding to the excitation of 3p states), and O-K (corresponding to the excitation of the 1s state) are resolved. The spectra of the BaSnO<sub>3</sub> (red curve) and La:BaSnO<sub>3</sub> (green curve) are very similar, apart from the presence of La peaks in the latter. Very importantly, this similarity is observed in the area around the Sn-M<sub>4,5</sub> edge [see inset Fig. 2], as well as around the O-K edge (energy range 530 – 560 eV). The line shape of the Sn-M<sub>4,5</sub> features is comparable to that reported for SnO<sub>2</sub> and La:BaSnO<sub>3</sub>, suggesting an oxidation state of 4+ for the Sn ions in the layers for both undoped and La-doped regions [33, 54]. Additionally, the O-K EELS spectral regions are consistent with those reported for stoichiometric BaSnO<sub>3</sub> and La:BaSnO<sub>3</sub> films [33, 55], which indicate no oxygen deficiency in the samples.

Figure 3 represents the XPS spectra of the Ba 3d core electrons together with the Voigt function fits. The Ba 3d spectra of all the samples showed an asymmetric line shape, suggesting the presence of multiple components in the core level. Two symmetric Voigt doublets (Ba I and Ba II) were used to fit the spectra. The main dou-

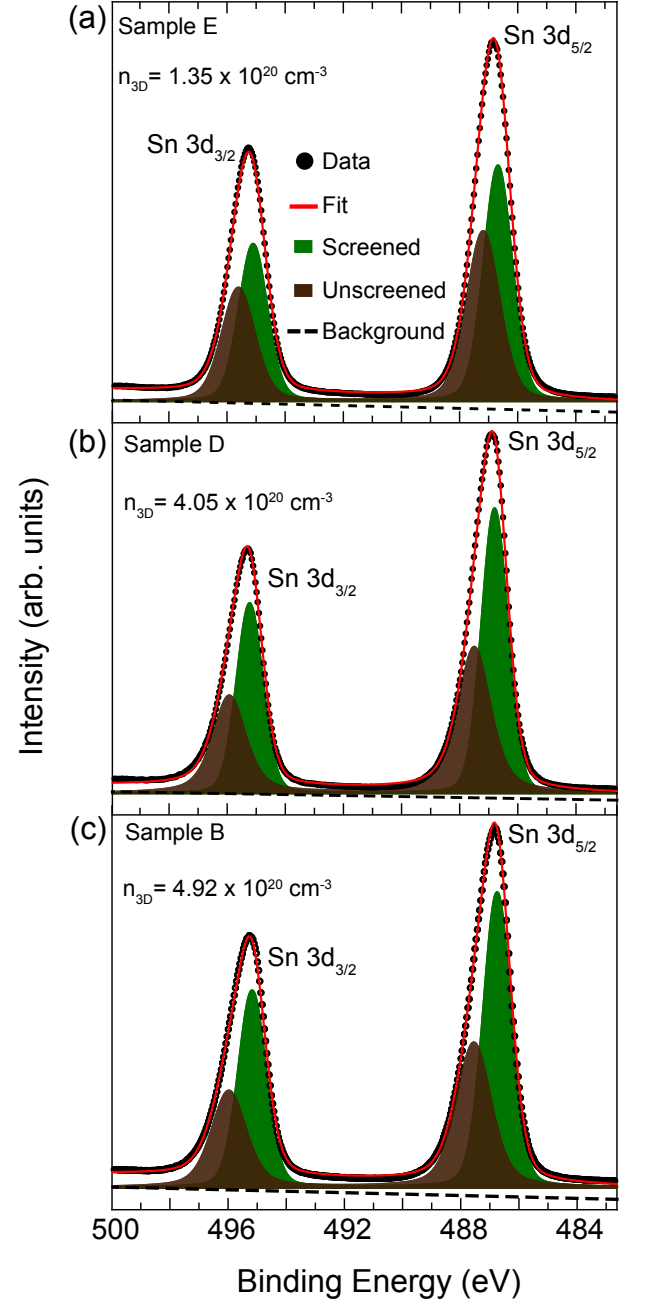


FIG. 4. XPS spectra around the Sn 3d regions for three samples of different total carrier density: (a) Sample E with  $n_{3D} = 1.35 \times 10^{20} \text{ cm}^{-3}$ , (b) Sample D with  $n_{3D} = 4.05 \times 10^{20} \text{ cm}^{-3}$ , and (c) Sample B with  $n_{3D} = 4.92 \times 10^{20} \text{ cm}^{-3}$ . After subtracting a Shirley background (black dashed lineshape), the Sn 3d spectra are fitted (red lineshape) with two Voigt doublet components. The data were acquired at normal emission with the Al K $\alpha$  excitation source. The peak heights were normalized for clarity.

blet, Ba I, located at the binding energy of 780.00 eV, is assigned to lattice barium in the Ba<sup>2+</sup> state, consistent with previous spectroscopic results on powder and epitaxial thin films of BaSnO<sub>3</sub> [56, 57]. The second dou-



TABLE II. Fitted parameters of the Sn 3d regions along with the calculated carrier density in each sample.

Sample name	Peak assignment	Peak position ( $\pm 0.05$ eV)	FWHM ( $\pm 0.05$ )	Relative intensity ( $\pm 1\%$ )	Satellite energy (eV)	Carrier density ( $\times 10^{20}$ cm $^{-3}$ )
E	Screened	486.68	1.15	54	0.5	$1.35 \pm 0.02$
	Unscreened	487.19	1.34	46		
D	Screened	486.80	1.06	57	0.7	$4.05 \pm 0.05$
	Unscreened	487.50	1.34	43		
B	Screened	486.75	1.12	60	0.8	$4.92 \pm 0.05$
	Unscreened	487.55	1.40	40		

blet, Ba II, situated at higher binding energy (781.13 eV), has been attributed to a surface character in several reports on epitaxial BaTiO<sub>3</sub> films [58–60]. This component was suggested to originate either from under-coordinated barium at a BaO terminated surface, or from lattice relaxation [59, 60].

In comparing the XPS spectra for cleaned surfaces with those of surfaces measured as-inserted [see Fig. S3 of the supplemental information], the relative intensity of Ba II was observed to decrease after the treatment of the surfaces, while that of Ba I increases. This trend suggests that Ba II could be a surface component, which is amplified with contamination. The nature of the Ba II peak was carefully investigated by carrying out a systematic analysis of its fraction with respect to the probing depth. This was achieved by performing angle-dependent XPS measurements as depicted in Fig. 3. The measurements were first performed using the Al K $_{\alpha}$  anode (photon energy of 1486.71 eV) at electron take-off angles of 35° [Fig. 3(a)] and 90° (normal emission) [Fig. 3(b)], and later the excitation source was changed to Ag L $_{\alpha}$  anode (photon energy of 2984.31 eV) for acquisition at normal emission [Fig. 3(c)]. For the take-off angle of 35°, the photoelectrons emitted originate from a region nearer the surface, whereas at the take-off angle of 90°, the emitted photoelectrons are from a deeper depth within the sample. Hence, the measurement gets more bulk sensitive as the photoelectron take-off angle increases from 35° to 90°, and as the excitation source is changed from Al to Ag. The parameters of the fits pertaining to the angle-dependent analysis are given in Table I. The ratio of the Ba II feature was observed to decrease considerably with bulk sensitivity measurements, thus confirming its surface character.

Two satellite features labeled Sat I and Sat II were also detected in the XPS spectra around the Ba 3d peaks [Fig. 3]. These satellites result from shake-up processes involving Ba 3d photoelectrons and valence electrons [61, 62]. These broad satellites are located about 10 eV on the high binding energy side of the associated Ba 3d $_{5/2}$  and Ba 3d $_{3/2}$  peaks.

Figure 4 depicts the Sn 3d core level XPS spectra for

three samples of different total carrier density. The Sn 3d spectral lineshapes display an asymmetry to the high binding energy side of the peak, which increases with increasing carrier density. In metallic systems, the asymmetry in core photoemission spectra arises from intrinsic plasmon excitations associated with the creation of the core hole, which results in an additional component satellite to the main core line [63, 64]. It is known that the Coulomb potential of the core hole creates a localized trap state by capturing a conduction electron [65–67]. In La:BaSnO<sub>3</sub> systems, the conduction band is derived from highly dispersive Sn 5s bands [32, 43], and the observed doping effect in the Sn 3d core level lineshape is most probably due to screening responses of the conduction electrons introduced by doping [63]. Therefore, two doublet components were used to fit the Sn 3d spectra assuming that the Koopmans’ state (excited state after the removal of a core electron from the atom) is projected into screened and unscreened final eigenstates [63].

To understand the effect of increasing carrier density in the Sn 3d core level, the spectral lineshape of three samples (B, D and E) of different  $n$  values were studied as portrayed in Fig. 4. The core lines were fitted to two Voigt components, which give an excellent description of the overall line shape of the spectra. In each spectrum, the main component is the peak at low binding energy labeled “screened”. This peak has a dominant Gaussian line shape. The component at high binding energy labeled “unscreened” is dominantly Lorentzian, which is a satellite associated with intrinsic plasmon excitations. Similar satellite structures were reported in the Sn 3d and In 3d core photoemission spectra of binary transparent conducting oxides (Sb-doped SnO<sub>2</sub> [63, 64, 68], In<sub>2</sub>O<sub>3</sub>–ZnO [69] and Sn-doped In<sub>2</sub>O<sub>3</sub> [67, 70]). Table II summarizes the fit parameters. As can be seen, the binding energy value of the main component suggests a valence state of 4+ for Sn [73, 74]; and the energy separation (satellite energy) between the main and satellite components increases with  $n$ . Furthermore, the relative intensity of the screened component increases with increasing  $n$ , while that of the unscreened peak decreases. This observation is in agreement with the Langreth model

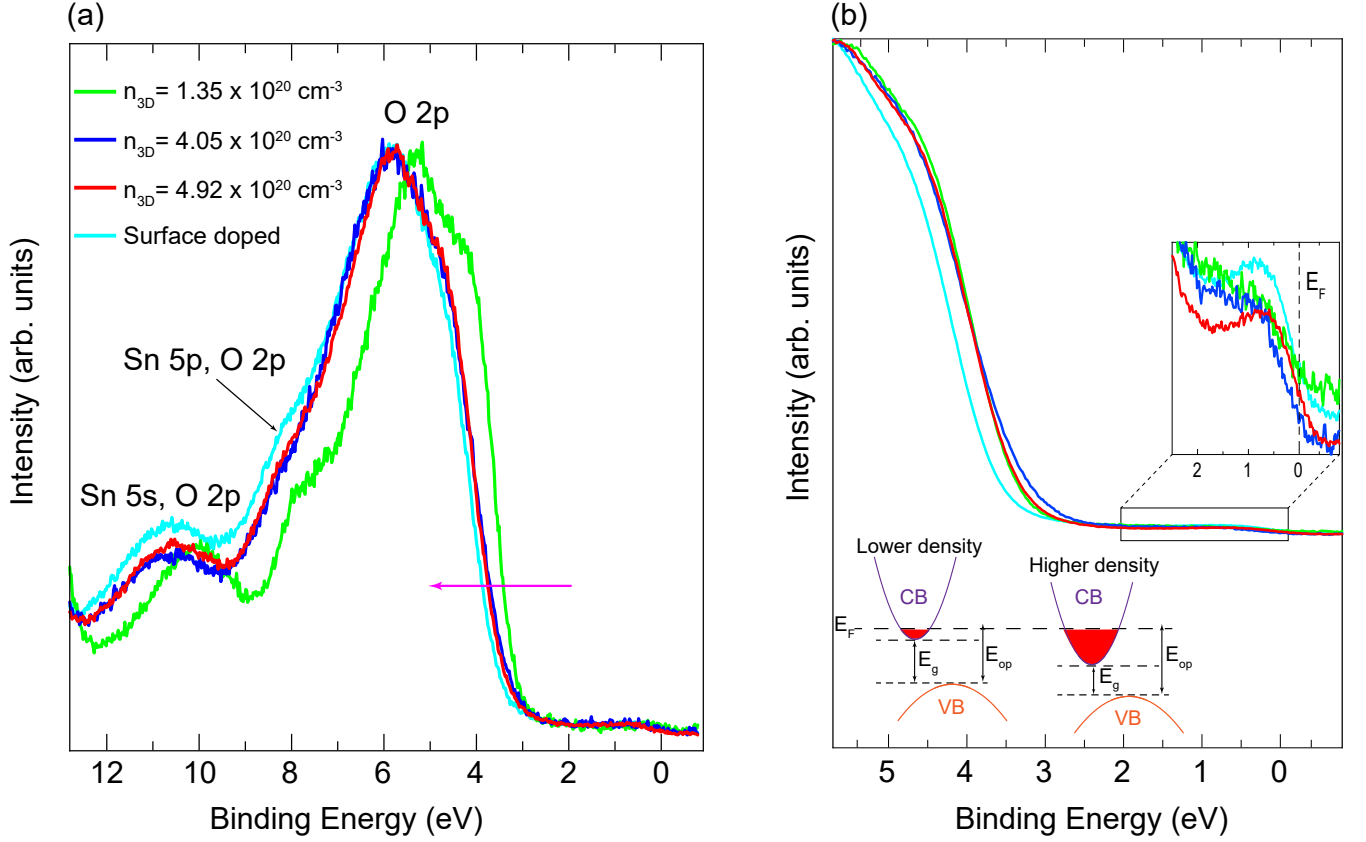


FIG. 5. (a) XPS valence band spectra of three samples of different total carrier density excited with the Al  $K\alpha$  anode: Sample E (green curves), Sample D (blue curves), and Sample B (red and cyan curves). To investigate how surface absorbed carbonate and hydroxide layers affect the states in the valence band region, after initial measurements of the core levels and valence band spectra, the sample B (cyan curve, surface doped) was intentionally exposed to contamination in the loadlock chamber operated at  $1 \times 10^{-8}$  mbar (not UHV). The carrier densities of all the samples are indicated. The blue, green and cyan curves are normalized to the maximum intensity of the red curve. The magenta arrow indicates the shift of the valence band with increasing carrier density. (b) Magnified view of the low energy part of the spectra on (a). The bottom left inset is a schematic illustration of the Moss-Burstein shift [71, 72], which shows how the doping process affects the electronic band structure of the material. The top right inset is enlarged spectra for the region around the Fermi level.

[65, 75]. In addition, the screened peak is narrower than the unscreened component as evidenced by their FWHM values. For fitting the spectra, the Gauss-Lorentz ratio was allowed to vary freely. Boundaries were set for the satellite energy. These constraints were applied to the lower limit of the position of the unscreened peak with the consideration that the satellite energy corresponds to the plasmon energy (i.e., the surface plasmon energy) and increases with the carrier density [63, 64, 67, 76, 77]. Since the surface plasmon energy is proportional to the carrier density [64, 70], the constraints were such that the satellite energy would be in the range of values reported for photoemission spectra of the 3d orbitals in binary transparent conducting oxides [63, 64, 67, 69] with comparable  $n$  values as in samples B, D and E. Therefore, the consistent observation of a narrower low binding energy peak and a broader high binding energy peak supports the applicability of the plasmon model to the analysis of the Sn 3d core XPS spectra in these films, which is con-

sistent with previously reported Sn 3d core level spectra in Sb-doped  $\text{SnO}_2$  samples [63, 64, 68].

Next, we explore the effect of increasing carrier density on the valence and conduction band spectra. The same La:BaSnO<sub>3</sub> samples characterized for the core level spectra were used. The XPS spectra of the valence and conduction bands are depicted in Figs. 5(a) and 5(b), respectively. Three main features are observed in the valence band spectra: (i) a mixture of Sn 5s and bonding O 2p orbitals located at 10.6 eV; (ii) the states at 8.3 eV originating from hybridized Sn 5p and O 2p orbitals; and (iii) the bands at binding energies between 4 and 6 eV associated with O 2p bonding or anti-bonding character [78–80]. Additionally, shifts of the valence band leading edge to high binding energies upon increasing carrier density can be observed. This indicates an increase in the optical band gap as proposed previously in ellipsometry and HAXPES results [25, 32, 81]. These shifts are correlated to the shifts observed in the core levels [See

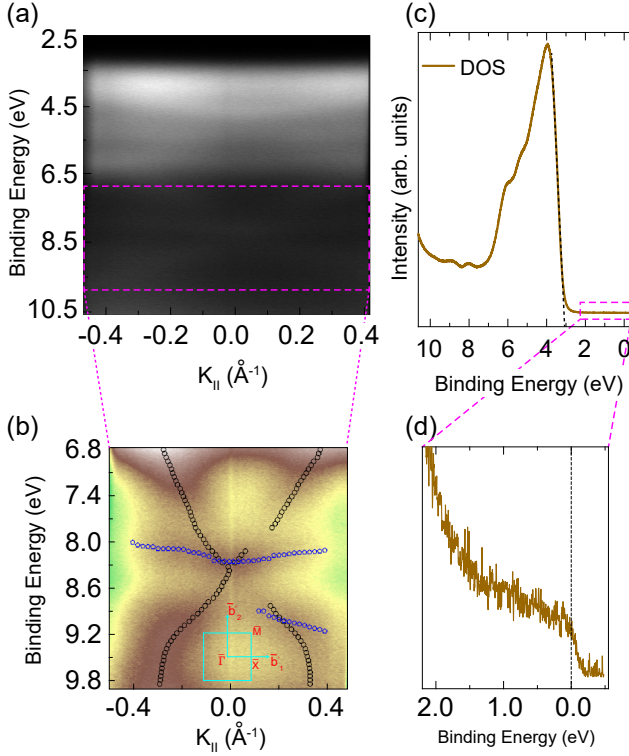


FIG. 6. (a) Representative 2D ARPES map for the Sample E. The map was acquired in the  $\bar{\Gamma} - \bar{X}$  direction. (b) ARPES map of the region indicated by the pink dashed rectangle. The inset shows the first Brillouin zone together with the  $\bar{\Gamma}$ ,  $\bar{X}$  and  $\bar{M}$  high symmetry points. (c) A representative density of states (DOS) integrated over the entire momentum space from the ARPES map in (a). The black dashed line is a linear extrapolation of the valence band leading edge, revealing that the valence band maximum is located at  $\sim 3.1$  eV. (d) Enlargement of the region around the Fermi level in (c).

supplementary information], as well as to the increasing asymmetry in the Sn 3d core lines. Similar trends were observed in other degenerate doped transparent conducting oxides, which were attributed to the increasing occupation of the states in the conduction band [63, 67, 69]. It is noteworthy that an opposite trend (i.e., shift of the valence band spectra toward lower binding energies with increases in La doping) was reported in recent angle resolved photoemission spectroscopy (ARPES) experiments on La:BaSnO<sub>3</sub> films, and it was suggested to originate from the opposite evolution of surface and bulk chemical potentials [46].

To explore further spectral features arising from occupation of the conduction bands, high resolution scans around the valence band leading edges were acquired [Fig. 5(b)]. In order to achieve an adequate signal to noise ratio and resolve the fine features in the region close to the Fermi energy ( $E_F$ ), each spectrum was acquired over a period of about 20 hours. A peak at  $\sim 4$  eV deriving from O 2p orbitals is observed in all spec-

tra as indicated by their first derivatives [see Fig. S5 of the supplementary information] [45, 46]. For the contaminated surface (sample with the highest  $n$  intentionally exposed to contamination in the load lock), a shift to higher binding energy of  $\sim 0.23$  eV is clearly visible in the leading edge valence band spectrum [see cyan curve in Fig. 5(b)]. Furthermore, a bump is detectable in all spectra in the region between 2 eV and  $E_F$  [see top right inset in Fig. 5(b)]. The spectra exhibit a weak structure close to  $E_F$ , which terminates in a sharp Fermi edge. This structure is associated with occupied states in the conduction band (Sn 5s orbital character with a small contribution from O 2p orbitals) [32, 43]. Moreover, the intensity of this CBM peak is observed to increase in the contaminated surface as evidenced by the cyan curve [see top right inset in Fig. 5(b)]. This suggests that exposure of the surface to contamination results in increasing occupied states in the conduction band. We attribute this behavior to the Moss-Burstein effect, i.e., the apparent optical band gap of the material is increased as the absorption edge is pushed to higher energies as a result of some states close to the conduction band being populated [see, bottom left inset in Fig. 5(b)] [71, 72]. Indeed, the valence band shifts associated with the increasing density of electrons occupying the conduction band were reported in several transparent conducting oxides, resulting in the increase of the intensity of the conduction band feature [25, 32, 67, 69, 82].

To date, few ARPES studies of the electronic band structure of La:BaSnO<sub>3</sub> and BaSnO<sub>3</sub> films have been reported [44–46]. In Fig. 6, we present the ARPES data of the band structure of a representative La:BaSnO<sub>3</sub> film exposed to air for days [83]. These data were collected at room temperature. Although ARPES is a very surface sensitive technique and the samples were exposed to ambient conditions, valence band dispersion are observed from about 3.10 to 10.62 eV [Fig. 6(a)]. The fact that these bands are not clearly resolved is understood in terms of the need for a very particular surface treatment associated with *ex-situ* ARPES measurements [44]. Figure 6(b) depicts a high-resolution 2D ARPES map in the binding energies ranging from 6.8 to  $\sim 9.8$  eV around the hybridized Sn 5s and O 2p states. Some highly dispersive bands are resolved: the black markers overlaying the dispersing bands are extracted band dispersions obtained from peak fitting of the momentum distribution curves (MDCs), whereas the blue markers are for bands fitted to peaks in the energy distribution curves (EDCs). Figure 6(c) represents the density of states (DOS) integrated from the ARPES map (i.e., EDC obtained from the ARPES map over the entire momentum space). The DOS spectrum exhibits well resolved band features that are similar to the XPS valence band spectra [Fig. 5(a)]. The Fermi-Dirac edge straddling at 0 eV is visible [Fig. 6(d)], and a linear extrapolation of the valence band leading edge reveals that the VBM is situ-

ated at  $\sim 3.1$  eV [see, black dashed line in Fig. 6(c)]. The extracted VBM value is in close agreement to previous theoretical and experimental values [43–46].

In summary, we have systematically investigated the evolution of electronic states in the band structure of La:BaSnO<sub>3</sub> films at different La doping levels. A close connection between the transport and the spectroscopic characteristics is demonstrated. In particular, increasing the carrier concentration in the conduction band by doping is observed to significantly affect the core and valence band spectra. The Sn 3d core line shape presents a pronounced asymmetry variation with the carrier density, and is fitted following the plasmon model applicable to metallic systems. Scans around the valence band spectra allowed the detection of the occupied states in the conduction bands. It is determined that surface contamination could potentially induce surface carrier accumulation, supported by the increase in the intensity of the CBM detected in the surface exposed to contamination. This study presents a detailed characterization the chemical composition of the near-surface region of La:BaSnO<sub>3</sub>, and it provides a better picture of the interplay between the doping concentration, electronic band structure and transport properties of epitaxial La:BaSnO<sub>3</sub> films.

B. P. Doyle, A. P. Nono Tchiomo, A. R. E. Prinsloo and E. Carleschi acknowledge funding support from the National Research Foundation (NRF) of South Africa under Grant Nos. 93205, 90698, 99030, and 111985. W. Sigle and P. van Aken acknowledge funding from the European Union's Horizon 2020 research and innovation programme under grant agreement No. 823717-ESTEEM3.

---

\* corresponding author, [p.ngabonziza@fkf.mpg.de](mailto:p.ngabonziza@fkf.mpg.de)

† corresponding author, [bpdoyle@uj.ac.za](mailto:bpdoyle@uj.ac.za)

- [1] H. J. Kim, U. Kim, H. M. Kim, T. H. Kim, H. S. Mun, B.-G. Jeon, K. T. Hong, W.-J. Lee, C. Ju, K. H. Kim, and K. Char, *Appl. Phys. Express* **5**, 061102 (2012).
- [2] H. J. Kim, U. Kim, T. H. Kim, J. Kim, H. M. Kim, B.-G. Jeon, W.-J. Lee, H. S. Mun, K. T. Hong, J. Yu, K. Char, and K. H. Kim, *Phys. Rev. B* **86**, 165205 (2012).
- [3] X. Luo, Y. S. Oh, A. Sirenko, P. Gao, T. A. Tyson, K. Char, and S.-W. Cheong, *Appl. Phys. Lett.* **100**, 172112 (2012).
- [4] W.-J. Lee, H. J. Kim, J. Kang, D. H. Jang, T. H. Kim, J. H. Lee, and K. H. Kim, *Annu. Rev. Mater. Res.* **47**, 391 (2017), and references therein.
- [5] U. Kim, C. Park, T. Ha, Y. M. Kim, N. Kim, C. Ju, J. Park, J. Yu, J. H. Kim, and K. Char, *APL Mater.* **3**, 036101 (2015).
- [6] J. Yue, A. Prakash, M. C. Robbins, S. J. Koester, and B. Jalan, *ACS Appl. Mater. Interfaces* **10**, 21061 (2018).
- [7] Z. Wang, H. Paik, Z. Chen, D. A. Muller, and D. G. Schlom, *APL Mater.* **7**, 022520 (2019).
- [8] Y. Zhang, M. P. K. Sahoo, and J. Wang, *Phys. Chem. Chem. Phys.* **19**, 7032 (2017).
- [9] S. S. Shin, J. S. Kim, J. H. Suk, K. D. Lee, D. W. Kim, J. H. Park, I. S. Cho, K. S. Hong, and J. Y. Kim, *ACS Nano* **7**, 1027 (2013).
- [10] J. Park, U. Kim, and K. Char, *Appl. Phys. Lett.* **108**, 092106 (2016).
- [11] E. Fortunato, D. Ginley, H. Hosono, and D. C. Paine, *MRS Bulletin* **32**, 2007 (2016).
- [12] J. Li, Z. Ma, R. Sa, and K. Wu, *RSC Adv.* **7**, 32703 (2017).
- [13] P. Rajasekaran, M. Arivanandhan, Y. Kumaki, R. Jayavel, Y. Hayakawa, and M. Shimomura, *CrytEngComm.* **22**, 5363 (2020).
- [14] T. Wu and P. Gao, *Materials* **11**, 999 (2018).
- [15] H. J. Cho, B. Feng, T. Onozato, M. Wei, A. V. Sanchela, Y. Ikuhara, and H. Ohta, *Phys. Rev. Materials* **3**, 094601 (2019).
- [16] S. Ismail-Beigi, F. J. Walker, S.-W. Cheong, K. M. Rabe, and C. H. Ahn, *APL Materials* **3**, 062510 (2015).
- [17] K. Krishnaswamy, L. Bjaalie, B. Himmetoglu, A. Janotti, L. Gordon, and C. G. Van de Walle, *Appl. Phys. Lett.* **108**, 083501 (2016).
- [18] D. S. Ginley and C. Bright, *MRS Bulletin* **25**, 15 (2000).
- [19] A. Prakash, P. Xu, A. Faghaninia, S. Shukla, J. W. Ager, C. S. Lo, and B. Jalan, *Nat. Commun.* **8**, 15167 (2017).
- [20] U. S. Alaan, F. J. Wong, J. J. Ditto, A. W. Robertson, E. Lindgren, A. Prakash, G. Haugstad, P. Shafer, A. T. N'Diaye, D. Johnson, E. Arenholz, B. Jalan, N. D. Browning, and Y. Suzuki, *Phys. Rev. Materials* **3**, 124402 (2019).
- [21] A. V. Sanchela, M. Wei, H. Zensyo, B. Feng, J. Lee, G. Kim, H. Jeon, Y. Ikuhara, and H. Ohta, *Appl. Phys. Lett.* **112**, 232102 (2018).
- [22] H. J. Cho, T. Onozato, M. Wei, A. Sanchela, and H. Ohta, *APL Mater.* **7**, 022507 (2019).
- [23] S. Yu, D. Yoon, and J. Son, *Appl. Phys. Lett.* **108**, 262101 (2016).
- [24] D. Yoon, S. Yu, and J. Son, *NPG Asia Mater.* **10**, 363 (2018).
- [25] C. A. Niedermeier, S. Rhode, K. Ide, H. Hiramatsu, H. Hosono, T. Kamiya, and M. A. Moram, *Phys. Rev. B* **95**, 161202 (2017).
- [26] P. V. Wadekar, J. Alaria, M. O'Sullivan, N. L. O. Flack, T. D. Manning, L. J. Phillips, K. Durose, O. Lozano, S. Lucas, J. B. Claridge, and M. J. Rosseinsky, *Appl. Phys. Lett.* **105**, 052104 (2014).
- [27] A. P. Nono Tchiomo, W. Braun, B. P. Doyle, W. Sigle, P. van Aken, J. Mannhart, and P. Ngabonziza, *APL Mater.* **7**, 041119 (2019).
- [28] F.-Y. Fan, W.-Y. Zhao, T.-W. Chen, J.-M. Yan, J.-P. Ma, L. Guo, G.-Y. Gao, F.-F. Wang, and R.-K. Zheng, *Appl. Phys. Lett.* **113**, 202102 (2018).
- [29] H. Mizoguchi, P. Chen, P. Boolchand, V. Ksenofontov, C. Felser, P. W. Barnes, and P. M. Woodward, *Chem. Mater.* **25**, 3858 (2013).
- [30] K. Fujiwara, K. Nishihara, J. Shiogai, and A. Tsukazaki, *Appl. Phys. Lett.* **110**, 203503 (2017).
- [31] S. Raghavan, T. Schumann, H. Kim, J. Y. Zhang, T. A. Cain, and S. Stemmer, *APL Mater.* **4**, 016106 (2016).
- [32] Z. Lebens-Higgins, D. O. Scanlon, H. Paik, S. Sallis, Y. Nie, M. Uchida, N. F. Quackenbush, M. J. Wahila, G. E. Sterbinsky, D. A. Arena, J. C. Woicik, D. G. Schlom, and L. F. J. Piper, *Phys. Rev. Lett.* **116**, 027602 (2016).



- (2016).
- [33] H. Paik, Z. Chen, E. Lochocki, A. Seidner H., A. Verma, N. Tanen, J. Park, M. Uchida, S. Shang, B.-C. Zhou, M. Brützmam, R. Uecker, Z.-K. Liu, D. Jena, K. M. Shen, D. A. Muller, and D. G. Schlom, *APL Mater.* **5**, 116107 (2017).
  - [34] H. Wang, A. Prakash, K. Reich, K. Ganguly, B. Jalan, and C. Leighton, *APL Mater.* **8**, 071113 (2020).
  - [35] W. M. Postiglione, K. Ganguly, H. Yun, J. S. Jeong, A. Jacobson, L. Borgeson, B. Jalan, K. A. Mkhoyan, and C. Leighton, *Phys. Rev. Materials* **5**, 044604 (2021).
  - [36] R. Zhang, X. Li, J. Bi, S. Zhang, S. Peng, Y. Song, Q. Zhang, L. Gu, J. Duan, and Y. Cao, *APL Mater.* **9**, 061103 (2021).
  - [37] K. Ganguly, A. Prakash, B. Jalan, and C. Leighton, *APL Mater.* **5**, 056102 (2017).
  - [38] K. Ganguly, P. Ambwani, P. Xu, J. S. Jeong, K. A. Mkhoyan, C. Leighton, and B. Jalan, *APL Mater.* **3**, 062509 (2015).
  - [39] Y. He, R. Wei, C. Zhou, W. Cheng, X. Ding, C. Shao, L. Hu, W. Song, X. Zhu, and Y. Sun, *Cryst. Growth Des.* **21**, 5800 (2021).
  - [40] A. Prakash, P. Xu, X. Wu, G. Haugstad, X. Wang, and B. Jalan, *J. Mater. Chem. C* **5**, 5730 (2017).
  - [41] W.-J. Lee, H. J. Kim, E. Sohn, T. H. Kim, J.-Y. Park, W. Park, H. Jeong, T. Lee, J. H. Kim, K.-Y. Choi, and K. H. Kim, *Appl. Phys. Lett.* **108**, 082105 (2016).
  - [42] D. O. Scanlon, *Phys. Rev. B* **87**, 161201 (2013).
  - [43] S. Sallis, D. O. Scanlon, S. C. Chae, N. F. Quackenbush, D. A. Fischer, J. C. Woicik, J.-H. Guo, S. W. Cheong, and L. F. J. Piper, *Appl. Phys. Lett.* **103**, 042105 (2013).
  - [44] S. Soltani, S. Hong, B. Kim, D. Kim, J. K. Jung, B. Sohn, T. W. Noh, K. Char, and C. Kim, *Phys. Rev. Materials* **4**, 055003 (2020).
  - [45] B. S. Joo, Y. J. Chang, L. Moreschini, A. Bostwick, E. Rotenberg, and M. Han, *Curr. Appl. Phys.* **17**, 595 (2017).
  - [46] E. B. Lochocki, H. Paik, M. Uchida, D. G. Schlom, and K. M. Shen, *Appl. Phys. Lett.* **112**, 181603 (2018).
  - [47] W. Braun, M. Jäger, G. Laskin, P. Ngabonziza, W. Voesch, P. Wittlich, and J. Mannhart, *APL Mater.* **8**, 071112 (2020).
  - [48] P. Ngabonziza, M. P. Stehno, H. Myoren, V. A. Neumann, G. Koster, and A. Brinkman, *Adv. Electron. Mater.* **2**, 1600157 (2016).
  - [49] P. Ngabonziza, Y. Wang, and A. Brinkman, *Phys. Rev. Materials* **2**, 044204 (2018).
  - [50] P. Ngabonziza, *Nanotechnology* **33**, 192001 (2022).
  - [51] A. P. Nono Tchiomo, G. Babu-Geetha, E. Carleschi, P. Ngabonziza, and B. P. Doyle, *Surf. Sci. Spectra* **25**, 024001 (2018).
  - [52] M. A. V. Hove and S. Y. Tong, *Surface crystallography by LEED: theory, computation and structural results*, (Springer, Berlin, 1979).
  - [53] H. Mizoguchi, H. W. Eng, and P. M. Woodward, *Inorg. Chem.* **43**, 1667 (2004).
  - [54] M. S. Moreno, R. F. Egerton, and P. A. Midgley, *Phys. Rev. B* **69**, 233304 (2004).
  - [55] W. Y. Wang, Y. L. Tang, Y. L. Zhu, J. Suriyaprakash, Y. B. Xu, Y. Liu, B. Gao, S.-W. Cheong, and X. L. Ma, *Sci. Rep.* **5**, 16097 (2015).
  - [56] G. Larramona, C. Gutiérrez, I. Pereira, M. R. Nunes, and F. M. A. da Costa, *J. Chem. Soc. Faraday Trans. 1* **85**, 907 (1989).
  - [57] H. M. I. Jaim, S. Lee, X. Zhang, and I. Takeuchi, *Appl. Phys. Lett.* **111**, 172102 (2017).
  - [58] J. E. Rault, G. Agnus, T. Maroutian, V. Pillard, P. Lecoeur, G. Niu, B. Vilquin, M. G. Silly, A. Bendounan, F. Sirotti, and N. Barrett, *Phys. Rev. B* **87**, 155146 (2013).
  - [59] X. L. Li, B. Chen, H. Y. Jing, H. B. Lu, B. R. Zhao, Z. H. Mai, and Q. J. Jia, *Appl. Phys. Lett.* **87**, 222905 (2005).
  - [60] X. L. Li, H. B. Lu, M. Li, Z. Mai, H. Kim, and Q. J. Jia, *Appl. Phys. Lett.* **92**, 012902 (2008).
  - [61] J. A. Colón Santana, *Quantitative Core Level Photoelectron Spectroscopy* (Morgan & Claypool Publishers, San Rafael, USA, 2015).
  - [62] G. B. Armen, T. Åberg, K. R. Karim, J. C. Levin, B. Crasemann, G. S. Brown, M. H. Chen, and G. E. Ice, *Phys. Rev. Lett.* **54**, 182 (1985).
  - [63] R. G. Egddell, J. Rebane, T. J. Walker, and D. S. L. Law, *Phys. Rev. B* **59**, 179 (1999).
  - [64] R. Egddell, T. Walker, and G. Beamson, *J. Electron Spectrosc. Relat. Phenom.* **128**, 59 (2003).
  - [65] J. N. Chazalviel, M. Campagna, G. K. Wertheim, and H. R. Shanks, *Phys. Rev. B* **16**, 697 (1977).
  - [66] M. Campagna, G. K. Wertheim, H. R. Shanks, F. Zumsteg, and E. Banks, *Phys. Rev. Lett.* **34**, 738 (1975).
  - [67] C. Körber, V. Krishnakumar, A. Klein, G. Panaccione, P. Torelli, A. Walsh, J. L. F. Da Silva, S.-H. Wei, R. G. Egddell, and D. J. Payne, *Phys. Rev. B* **81**, 165207 (2010).
  - [68] P. Cox, R. Egddell, C. Harding, A. Orchard, W. Patterson, and P. Tavener, *Solid State Commun.* **44**, 837 (1982).
  - [69] J. Jia, N. Oka, and Y. Shigesato, *J. Appl. Phys.* **113**, 163702 (2013).
  - [70] V. Christou, M. Etchells, O. Renault, P. J. Dobson, O. V. Salata, G. Beamson, and R. G. Egddell, *J. Appl. Phys.* **88**, 5180 (2000).
  - [71] E. Burstein, *Phys. Rev.* **93**, 632 (1954).
  - [72] T. S. Moss, *Proc. Phys. Soc. B* **67**, 775 (1954).
  - [73] W. E. Morgan and J. R. Van Wazer, *J. Phys. Chem.* **77**, 964 (1973).
  - [74] V. B. Crist, *Handbook of monochromatic XPS spectra: The elements of native oxides* (John Wiley & Sons, Chichester, 2000).
  - [75] D. C. Langreth, Theory of plasmon effects in high-energy spectroscopy, in *Proceedings of Nobel Symposium 24 in Medicine and Natural Science*, edited by B. Lundqvist and S. Lundqvist (Academic Press, New York and London, 1973) pp. 210–222.
  - [76] D. J. Payne, R. G. Egddell, W. Hao, J. S. Foord, A. Walsh, and G. W. Watson, *Chem. Phys. Lett.* **411**, 181 (2005).
  - [77] P.-A. Glans, T. Learmonth, K. E. Smith, J. Guo, A. Walsh, G. W. Watson, F. Terzi, and R. G. Egddell, *Phys. Rev. B* **71**, 235109 (2005).
  - [78] J. M. Themlin, R. Sporken, J. Darville, R. Caudano, J. M. Gilles, and R. L. Johnson, *Phys. Rev. B* **42**, 11914 (1990).
  - [79] S. K. Vasheghani Farahani, T. D. Veal, J. J. Mudd, D. O. Scanlon, G. W. Watson, O. Bierwagen, M. E. White, J. S. Speck, and C. F. McConville, *Phys. Rev. B* **90**, 155413 (2014).
  - [80] L. Kövér, G. Moretti, Z. Kovács, R. Sanjinés, I. Cserny, G. Margaritondo, J. Pálkás, and H. Adachi, *J. Vac. Sci. Technol. A* **13**, 1382 (1995).
  - [81] D. Seo, K. Yu, Y. Jun Chang, E. Sohn, K. Hoon Kim, and E. J. Choi, *Appl. Phys. Lett.* **104**, 022102 (2014).

- [82] J. J. Mudd, T.-L. Lee, V. Muñoz Sanjosé, J. Zúñiga Pérez, D. J. Payne, R. G. Egdell, and C. F. McConville, [Phys. Rev. B \*\*89\*\*, 165305 \(2014\)](#).
- [83] The La:BaSnO<sub>3</sub> films were prepared at the Max Planck Institute for Solid State Research, Stuttgart, Germany

and transported at ambient conditions for further spectroscopic measurements (XPS and ARPES) to the University of Johannesburg, South Africa. Details on the cleaning procedure of the samples and spectroscopic measurements are presented in supplementary information.

## Supplementary Information:

### Combined Spectroscopy and Electrical Characterizations of La:BaSnO<sub>3</sub> Thin Films and Heterostructures

Arnaud P. Nono Tchiomo,<sup>1,2</sup> Emanuela Carleschi,<sup>1</sup> Aletta R. E. Prinsloo,<sup>1</sup> Wilfried Sigle,<sup>3</sup> Peter A. van Aken,<sup>3</sup> Jochen Mannhart,<sup>3</sup> Prosper Ngabonziza,<sup>1,3,\*</sup> Bryan P. Doyle,<sup>1,‡</sup>

<sup>1</sup>*Department of Physics, University of Johannesburg, P.O. Box 524, Auckland Park 2006,  
Johannesburg, South Africa*

<sup>2</sup>*Van der Waals-Zeeman Institute, Institute of Physics, Science Park 904, 1098 XH Amsterdam,  
The Netherlands*

<sup>3</sup>*Max Planck Institute for Solid State Research, Heisenbergstr. 1, 70569 Stuttgart, Germany*

### Sample Characterizations and Electronic Transport Characteristics

After growth of La:BaSnO<sub>3</sub> films, Au/Ti contacts (45 nm thick) that provide electrical connections to the sample were added to the samples' corners using standard photolithography methods [Fig. S1(a)]. Basic electrical characterizations of the samples were performed using a physical property measurement system (PPMS) in four-point configuration with an excitation current of 1  $\mu$ A. Table S1 summarizes the transport characteristics of the La:BaSnO<sub>3</sub> films discussed in the main text.

The scanning transmission electron microscopy (STEM) and electron energy loss spectroscopy (EELS) investigations were performed using a Cs-probe-corrected JEOL JEM-ARM200F. The EELS measurements were performed on a cross-section of the sample, and the electron beam was focused on the BaSnO<sub>3</sub> buffer layer and the La:BaSnO<sub>3</sub> film layer regions. Spectra from areas without and with La could then be compared, to see whether the doping alters or changes the oxidation state of the Sn.

Low-energy electron diffraction (LEED) was used to analyze the surface structure and geometry of films that were cleaned in ultra-high vacuum (UHV). LEED characterizations were done in order to check the surfaces in the cleaning process prior to spectroscopic measurements, and for determination of the orientation of the surfaces before angle

TABLE S1. Electronic transport characteristics (carrier density and mobility) of the samples discussed in this study.

Sample name	Sample layout	Carrier density ( $\times 10^{20} \text{ cm}^{-3}$ )	Carrier mobility ( $\text{cm}^2 \text{ V}^{-1} \text{ s}^{-1}$ )
A	6% La:BaSnO <sub>3</sub> (25 nm)/BaSnO <sub>3</sub> (100 nm)/DyScO <sub>3</sub>	$1.24 \pm 0.02$	$71 \pm 2$
B	6% La:BaSnO <sub>3</sub> (25 nm)/BaSnO <sub>3</sub> (100 nm)/TbScO <sub>3</sub>	$4.92 \pm 0.05$	$20 \pm 1$
C	4% La:BaSnO <sub>3</sub> (25 nm)/BaSnO <sub>3</sub> (100 nm)/SrTiO <sub>3</sub>	$8.05 \pm 0.05$	$18.5 \pm 1$
D	6% La:BaSnO <sub>3</sub> (25 nm)/SrTiO <sub>3</sub>	$4.05 \pm 0.05$	$91 \pm 2$
E	2% La:BaSnO <sub>3</sub> (25 nm)/TbScO <sub>3</sub>	$1.35 \pm 0.02$	$75 \pm 2$

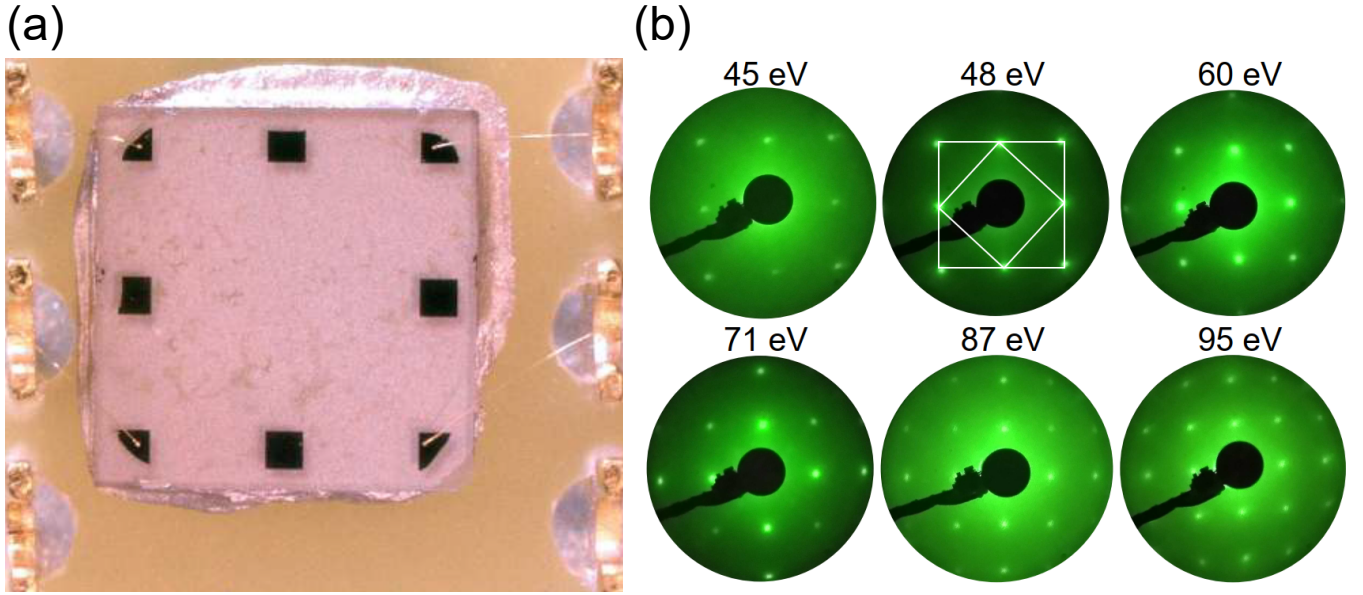


FIG. S1. (a) Optical photograph of a typical La:BaSnO<sub>3</sub> film structured in the Van der Pauw geometry, using metal contact pads of Au/Ti. The contacts are connected to the sample holder pins using aluminum wires bonds at the corners of the sample. (b) Representative LEED images of the La:BaSnO<sub>3</sub> (001) surface taken at various electron energies. The white squares drawn on the image recorded at 48 eV illustrates the square lattice of BaSnO<sub>3</sub>. Note that at the electron energy of 48 eV, the diffraction pattern shows only first order beams, and when the energy is approximately doubled (at 95 eV), second order spots are observed.

resolved photoemission spectroscopy (ARPES) measurements. Figure S1(b) and Fig. S2(a) depict representative LEED images of the La:BaSnO<sub>3</sub> (001) surface at different electron energies and at different stages in the high-temperature cleaning process, respectively.

### Photoemission Spectroscopy Measurements

The La:BaSnO<sub>3</sub> thin films and heterostructures were grown using pulsed laser deposition at the Max Planck Institute for Solid State Research, Stuttgart Germany. After electronic transport characterizations, samples were transported in ambient conditions to the University of Johannesburg in South Africa for further spectroscopic measurements. X-ray photoemission spectroscopy (XPS) and ARPES spectra were collected using a SPECS PHOIBOS 150 hemispherical electron energy analyzer. The base pressure in the analysis chamber during acquisition of the core and valence XPS data was  $\approx 3 \times 10^{-10}$  mbar. These were measured using monochromatized Al K $\alpha$  and Ag L $\alpha$  excitation sources, emitting photons of energies of 1486.71 eV and 2984.31 eV, respectively. The experimental resolutions with these two sources were 580 and 960 meV, respectively. To investigate the electronic band structure, we also excited the valence electrons of the samples using a He I source delivering photons of 21.2 eV. For these ARPES measurements, the experimental resolution was 120 meV.

As the samples had been exposed to air under ambient conditions, their surfaces were thoroughly cleaned in vacuum prior to spectroscopic measurements. The cleaning procedure consisted of annealing in O<sub>2</sub> environment at the temperature of  $\sim 700$  °C in a preparation chamber maintained at  $\approx 7 \times 10^{-6}$  mbar. The annealing procedure consisted of several cycles of 2 hours each and it was done using an e-beam heater at a maximum electron emission



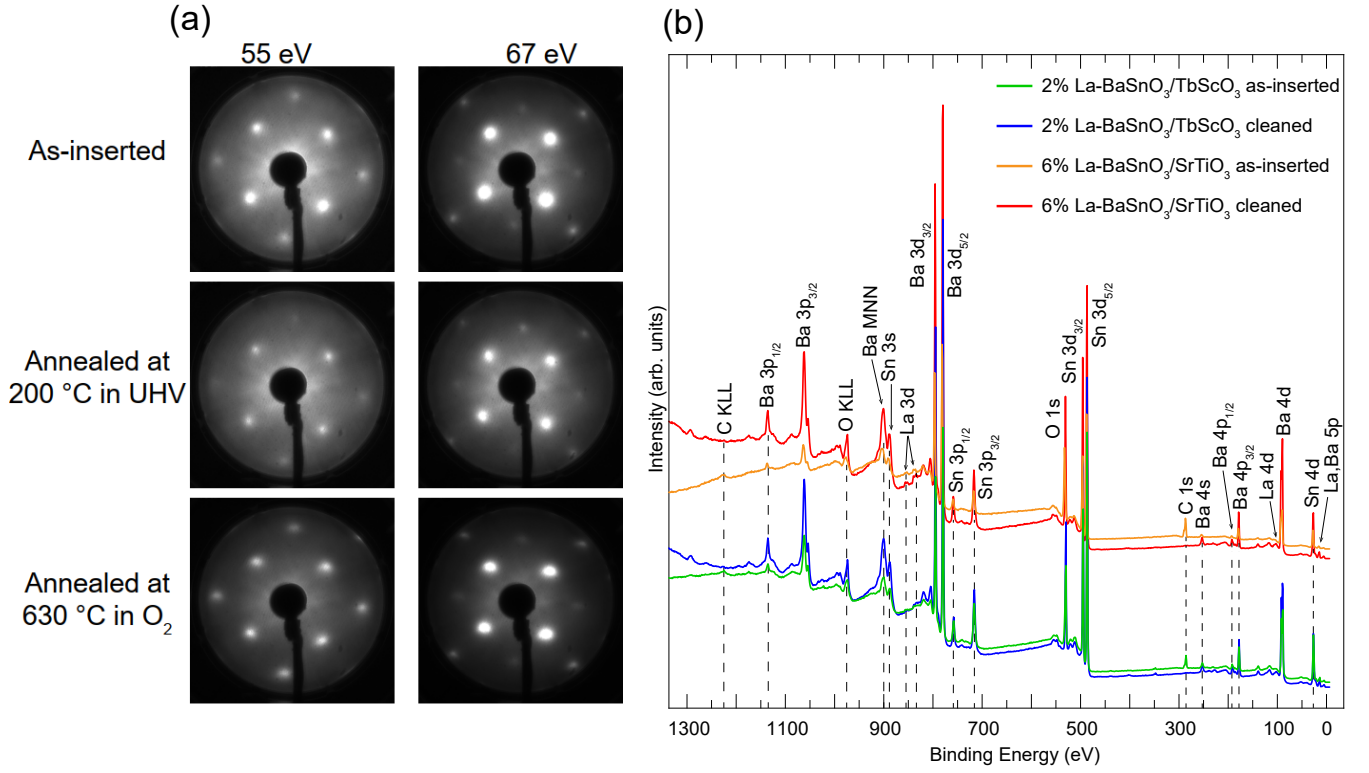


FIG. S2. (a) Representative LEED images from the surface of a La:BaSnO<sub>3</sub> (25 nm)/BaSnO<sub>3</sub> (100 nm)/TbScO<sub>3</sub> heterostructure. The images are taken at various electron energies on the surface at different stages of cleaning. (b) XPS survey scans for as-inserted (light green and orange curves) and cleaned (blue and red curves) for the samples E and D. All the core levels from La, Ba, Sn and O elements can be seen in the spectra. The C 1s signal originating from surface contamination with the associated C KLL Auger electron peak are also visible. The spectra were acquired with an experimental resolution of 0.90 eV using the Al K<sub>α</sub> excitation source.

power of 3.5 W. The temperature was indicated by a pyrometer set to an emissivity of 0.1. The cleanliness of the samples was monitored by recording the LEED patterns directly after an annealing cycle [Fig. S2(a)], as well as by tracking the C 1s signal in the XPS survey scans [Fig. S2(b)] and by tracking the O 1s, Sn 3d and Ba 3d before and after surface cleaning [see, Fig. S3, Fig. S4].

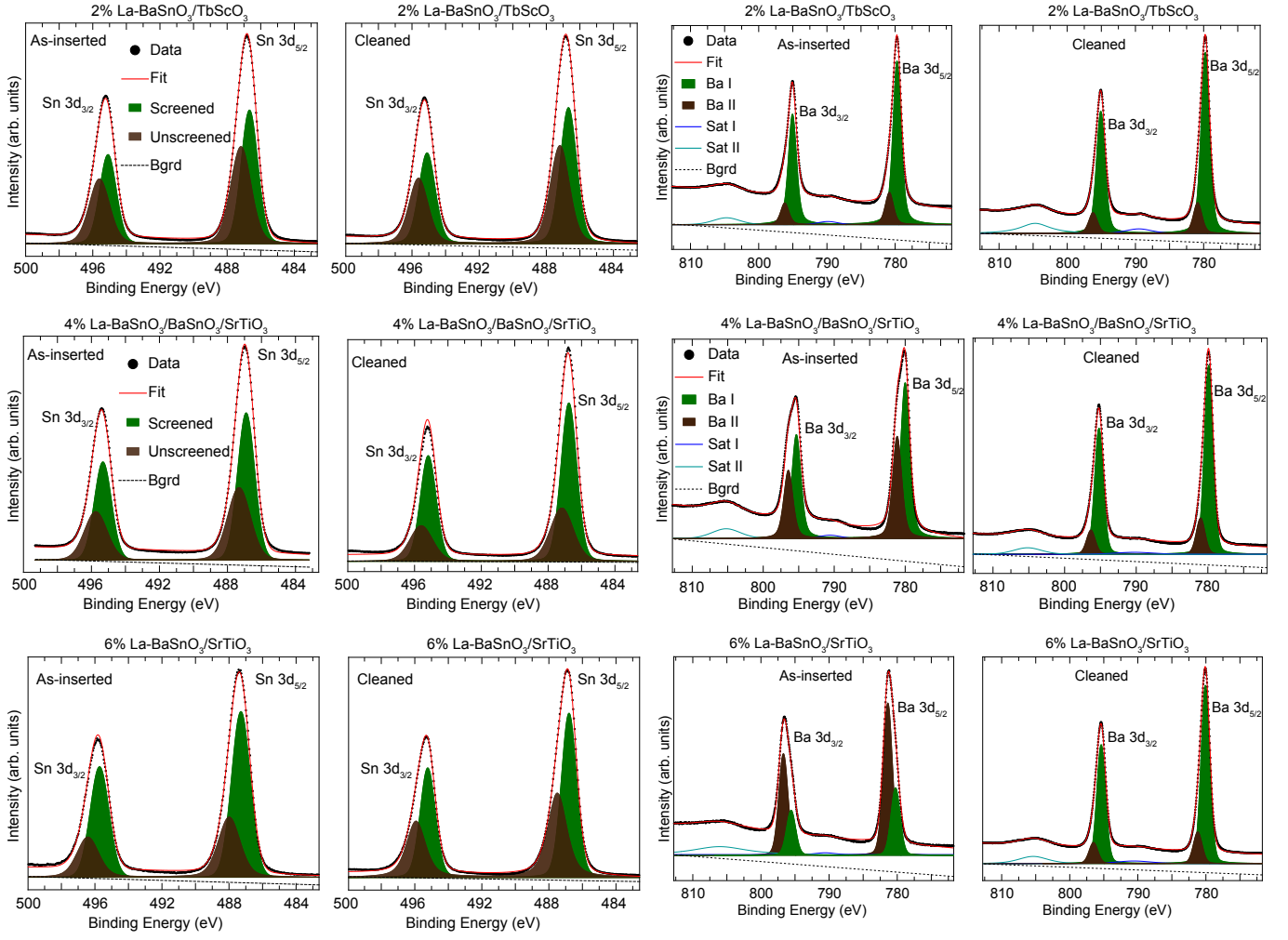


FIG. S3. Fits of the XPS spectra around the Sn 3d and Ba 3d regions for as-inserted and cleaned 2% La:BaSnO<sub>3</sub>/TbScO<sub>3</sub>, 4% La:BaSnO<sub>3</sub>/BaSnO<sub>3</sub>/SrTiO<sub>3</sub> and 6% La:BaSnO<sub>3</sub>/SrTiO<sub>3</sub> films heterostructures. The spectra were fitted with two Voigt doublets. The data were acquired with an experimental resolution of 0.78 eV

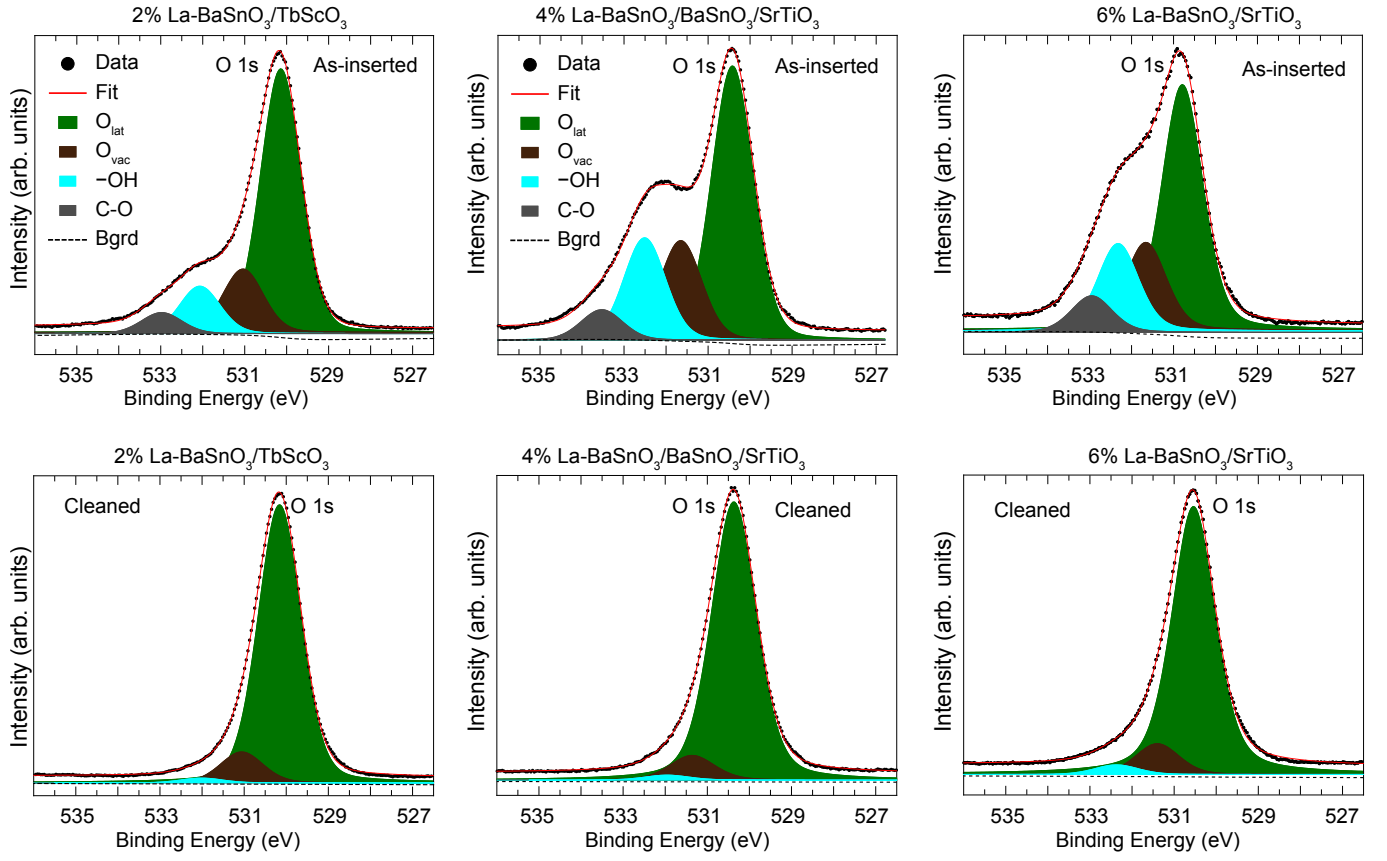


FIG. S4. Representative fits of the XPS spectra for the O 1s core levels for as-inserted and cleaned 2% La:BaSnO<sub>3</sub>/TbScO<sub>3</sub>, 6% La:BaSnO<sub>3</sub>/SrTiO<sub>3</sub> films and 4% La:BaSnO<sub>3</sub>/BaSnO<sub>3</sub>/SrTiO<sub>3</sub> heterostructures. The O 1s core electrons were fitted with four Voigt singlet components before cleaning, whereas three were used after vacuum cleaning steps.

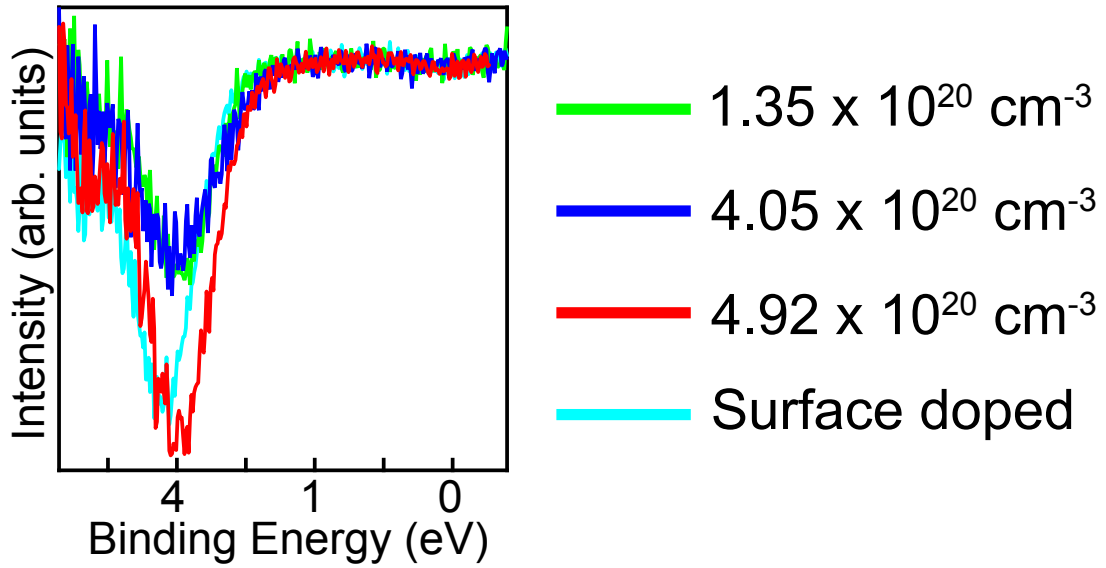


FIG. S5. First derivative of the XPS spectra discussed in Fig. 5 of the main text. The cyan curve is magnified  $\times 18$ , the blue and green curves are magnified  $\times 40$ .